Supporting Information for

Carbon supported noble metal nanoparticles as efficient catalysts for electrochemical water splitting

Meng Liu,[a] Ferdinand Hof,[b,c] Miriam Moro,[a] Giovanni Valenti,[a] Francesco Paolucci[a] and Alain Pénicaud *[b,c]

[a] Department of Chemistry "G. Ciamician", University of Bologna, via Selmi 2, 40126 Bologna, Italy.

[b] CNRS, Centre de Recherche Paul Pascal (CRPP), UMR 5031, F-33600 Pessac, France

[c] Université Bordeaux, CRPP, UMR 5031, F-33600 Pessac, France

Instruments:

X-ray powder diffraction (XRD). XRD patterns were collected on a Rigaku Nanoviewer (XRF microsourcegenerator, MicroMax007HF), with a 1200W rotating anode coupled to a confocal Max-FluxOsmic Mirror (Applied Rigaku Technologies, Austin, USA) and a MAR345 image plate detector (MARResearch, Norderstedt, Germany); samples were filled into glass capillaries and were exposed to the X-ray beam; the detector was placed at a distance of 156 mm providing access to 2q angles in the range between 0.9° and 48°.

Thermo gravimetric characterization (TGA). Thermo gravimetric characterization was performed on a TA Q50 TGA. Between 4-7 mg of composite sample was weighed in a Pt-crucible. The measurements were performed under synthetic air (80% N_2, 20% O_2) between 30-800 °C with a heating slope of 10°K/min.

X-ray photoelectron spectroscopy (XPS). A ThermoFisher Scientific K-ALPHA spectrometer was used for surface analysis with a monochromatized AlKα source (hv = 1486.6 eV) and a 200 microns spot size. A pressure of 10^{-7} Pa was maintained in the chamber during analysis. The full spectra (0-1150 eV) were obtained with constant pass energy of 200 eV and high-resolution spectra at constant pass energy of 40 eV. Charge neutralization was applied for all samples. High resolution spectra were fitted and quantified using the AVANTAGE software provided by ThermoFisher Scientific and the Scofield sensitivity factors available from the internal database.

Transmission electron microcopy (TEM). TEM measurements were performed on a TEM-FEG HR (JEOL 2200FS). TEM grids have been prepared by drop casting 20 μl of nanocomposite dispersion in THF directly onto SF400-CU TEM grids, silicon monoxide membranes on 400 mesh copper grids (Electron microscopy science).

Chemicals:

All chemicals were purchased from Sigma Aldrich. THF was purified prior use by means of Pure Solv 400-4-MD solvent purification system that is attached directly to the Glove box.

Carbon starting materials:

Graphitic nano carbon (nC):

Graphitic nano carbons have been obtained from FGV, Cambrige Nanosystems. The carbon is from synthetic origin by the microwave splitting of methane origin from bio resources, carbon content > 95 % and no inorganic impurities have been found by means of TGA measurement.

Synthesis

Synthesis of intercalation compound (A):

120 mg (10.0 mmol) of purified graphitic nano carbon (nC), generated through the plasma splitting of methane,[1] and 48.8 mg (1.25 mmol) cleaned potassium (stoichiometry KC_8) were placed together in a vial inside an argon filled glove box and heated for 5 hours at 180°C on a heating plate under occasional stirring. Afterwards, the vial was allowed to cool down to room temperature and the intercalated graphitic nano carbon (KC_8) was collected.

Safety remark:

The possible user of the presented synthetic protocol is reminded of the specific dangers related to the use of potassium metal. Safety precautions are advised for storage, handling and waste treatment.

Potassium metal is extremely dangerous in contact with water or moisture, releasing hydrogen with sufficient heat to cause ignition or explosion. Peroxide formation may occur in containers that have been opened and remained in storage. May produce corrosive solutions on contact with water.

Dispersion of intercalated nano carbon (KC_8) and isolation of the graphenide solution (B):

310 mg of the as prepared intercalated nano carbon (KC_8) were mixed with 75 mL of absolute THF under inert conditions in a 250 mL Erlenmeyer flask and the dispersion was stirred for 1 day by the aid of a glass coated magnetic stirring bar. Then the dispersion was centrifuged at 4500 rpm for 30 min under inert conditions and a dark / dark yellow upper solution was retained. The concentration of the graphenide solution was determined by dry extracts as 0.50 mg/mL ± 0.08 mg/mL.

Synthesis of the composite compound M(nP)/nC (C):

The as prepared graphenide solution has been used directly as reduction agent for the M(nP)/nC composite synthesis.

Equimolar amounts of anhydrous $PtCl_2$ or $RhCl_3$ chloride (specified in **Table ST1**) dispersed in 10 mL of absolute THF were added dropwise to 50 mL graphenide solution in a 250 mL Erlenmeyer flask inside an argon filled glove box. After 5-15 min, aggregation and precipitation occurred and the respective dispersion was stirred for 24 hours. Afterwards, the dispersion was removed from the glove box and 100 mL of deionized water was added to the dispersion under ambient conditions. The sample was purified by repeated centrifugation and re-dispersing steps (4 times, 1 h at 10000 rpm, 15300 g) and the final composite materials M(np)/nCs were isolated by freeze drying.

Table ST1 Synthesis details and amounts regarding the preparation of individual M(nP)/nC composite materials

	Volume of graphenide solution [mL]	**Weight of solvated intercalation compound [mg]**	**Amount of added metal salt [µmol]**	**Weight of added metal chloride [mg]**
Rh(nP)/nC ($RhCl_3$)	50	25	61.6	12.9
PtRh(nP)/nC ($PtCl_2$, $RhCl_3$)	50	25	46.2 ($PtCl_2$) 30.8 ($RhCl_3$),	12.3 ($PtCl_2$) 6.4 ($RhCl_3$),
Pt(nP)/nC ($PtCl_2$)	50	25	92.5	24.6

Electrochemical Measurement:

Electrochemical impedance spectroscopy (EIS) test was firstly conducted at open potential with frequency ranging from 0.1 Hz to 200 kHz before measuring electrocatalytic performance. Electrocatalytic activity was achieved from linear sweep voltammetry (LSV) polarization curves that were recorded at a scan rate of 5 mV s^{-1} while electrocatalytic stability was obtained from chronopotentiometry curves collected at a current density of 2 mA cm^{-2}. Moreover, a sequence of potential steps (200 seconds for each) under different overpotentials were carried out in order to achieve the turnover frequency (TOF), which refers to the number of moles of product per mole of catalyst per time unit. Besides, electrochemical specific surface areas (ECSAs) were investigated by means of cyclic voltammetry (CV) polarization curves within a potential range from 0 V to 1.0 V (vs reversible hydrogen electrode, RHE) at a scan rate 50 mV s^{-1}. All data were reported with iR drop compensation and all potentials were calibrated to RHE.

For this experiment, a specific three-electrode electrochemical cell was used, described in detail elsewhere.[2] The electrolysis was carried out in 4 mL of 0.1 M KOH. To saturate the system, Ar was continuously purged at a rate of 10 mL min^{-1} for least 30 minutes. Then, the flow was decreased to 5 mL min^{-1} for electrochemical measurements. The GC is of SRI Multiple Gas Analyser, equipped with one 6' Silica Gel column and one 6' Molecular Sieve 13X column. The columns are capable of simultaneously separating H_2, O_2, N_2, CO and hydrocarbons. During the experiments, the column temperature was maintained at 51°C. The GC has two detectors: thermal conductivity detector (TCD) and flame ionization detector (FID). The TCD consists of four tungsten-rhenium filaments in a Wheatstone bridge

configuration. Two of filaments are exposed only to carrier gas (Ar), which serves as a reference, while remaining two filaments are exposed to the carrier/sample flow. The FID has a unique ceramic ignitor which can run continuously and is kept isothermal in an aluminium block at 375°C. The FID is equipped with an electrometer amplifier, while the hydrogen and air gas flow are controlled using electronic pressure controllers (EPC).

Additional Physiochemical analysis:

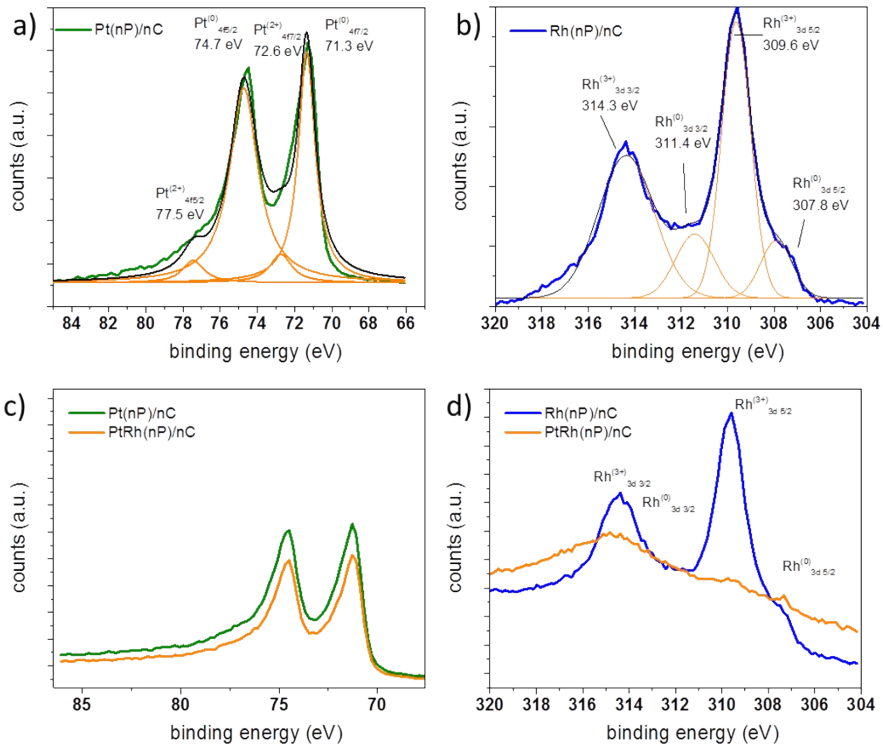

Figure S1 a) high resolution XPS spectra of the Pt(nP)/nC compound in the Pt_{4f} region and corresponding fits showing that the sample exhibits mainly metallic Pt with minor contributions of Pt^{2+}. b) high resolution XPS of the Rh(nP)/nC compound in the Rh_{3d} region and the corresponding fits show that mainly the sample contains Rh^{3+} with contributions of metallic Rh. c) comparison of the Pt(nP)/nC compound in the Pt_{4f} region with the PtRh(nP)/nC compound. d) comparison of Rh(nP)/nC compound in the Rh_{3d} region with the PtRh(nP)/nC compound.

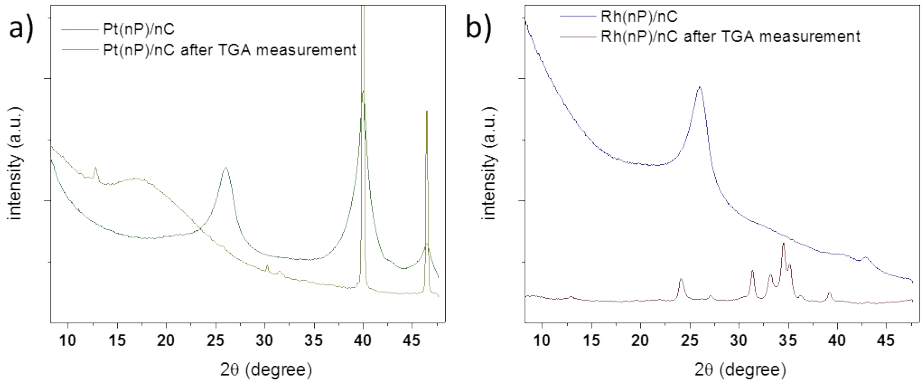

Figure S2 XRD patterns (CuKα) of a) the Pt(nP)/nC composite in comparison to the patterns from the solid residue material obtained after TGA measurements in synthetic air at 800°C; b) Rh(nP)/nC composite in comparison to the patterns from the solid residue material obtained after TGA measurements in synthetic air at 800°C. In both cases the peaks are narrower for the residue materials than for the composite materials. In case of the Pt(nP)/nC composite, after TGA measurement only metallic platinum particles remain which are orders of magnitude larger likely due to sintering effects. In case of the Rh(nP)/nC composite the resulting pattern exhibits various peaks that can be attributed to Rh_2O_3 and no traces of metallic rhodium is observable after TGA measurements at 800°C under synthetic showing the less noble character of the rhodium metal compared to the platinum one.

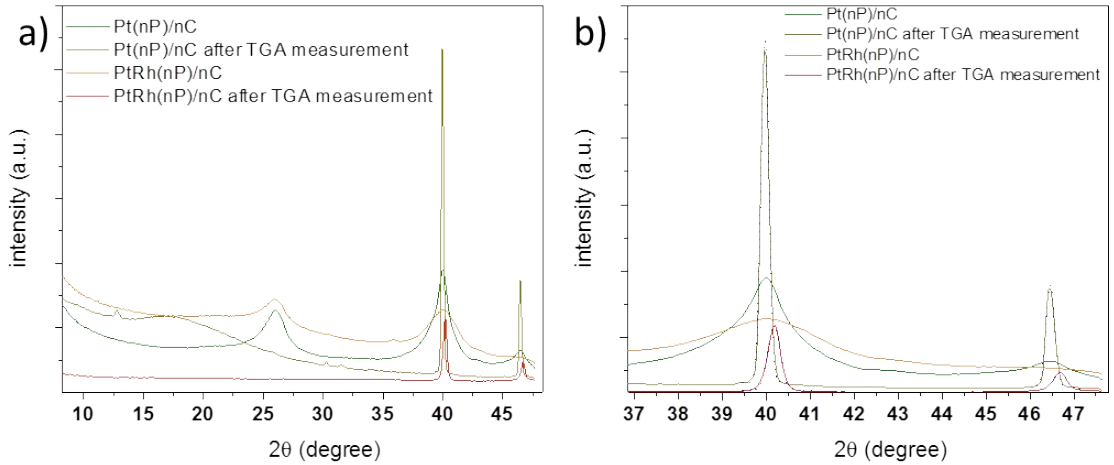

Figure S3 a*)* XRD patterns (CuKα) of the Pt(nP)/nC and the PtRh(nP)/nC composite materials in comparison to the patterns from the solid residue materials obtained after TGA measurements in synthetic air at 800°C; The patterns related to metallic nanoparticles in the residue material after TGA measurements can be clearly seen, which is a result of sintering processes at high temperature for both residue materials. In the PtRh(nP)/nC residue material there are no patterns visible that can be traced to Rh_2O_3 (see Fig. S2). b) enlargement of a), The peaks of the residue materials can be easily fitted and positions of 39.96, 46.46° (Pt residue compound, dark yellow trace) and 40.17°, 46.68° (RhPt residue compound, red trace) were found. By applying the Scherrer equation, 38 nm and 25 nm could be found for the residue compounds after TGA measurements respectively. The particle sizes of the Pt(nP)/nC and the PtRh(nP)/nC composite materials are about one order of magnitude smaller. Due to the broadening of the peaks and the sizes, the Scherrer equation may not be easily applied. By comparing the peak positions of the 2 residue compounds with the Pt(nP)/nC and the PtRh(nP)/nC composite materials, the observed difference in position is also present here. This difference can be related to a compressing of the metallic lattice, as observed by EXAFS data on RhPt nanoalloys.[3] Due to the similarity in behavior of those XRD patterns with ours, we believe that a nanoalloy is formed in our case, due to the simultaneous co-reduction of Rh^{3+} and Pt^{2+} in the synthesis step for the PtRh(nP)/nC compound.

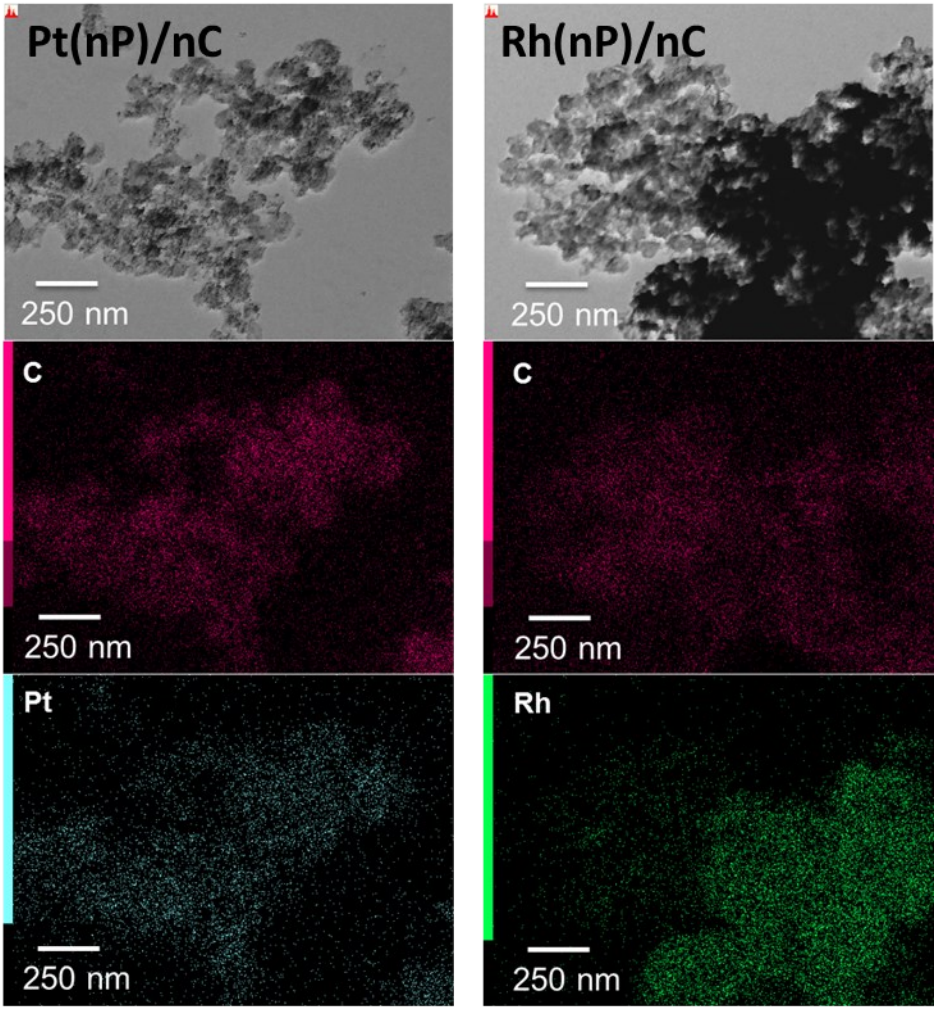

Figure S4 STEM/EDX mapping of the Pt(nP)/nC (left side) and Rh(nP)/nC (right side) composite materials. STEM images in the top, mapping of the carbon edge in the middle (red) and the respective metal edge Pt (blue, left side) and Rh (green, right side).

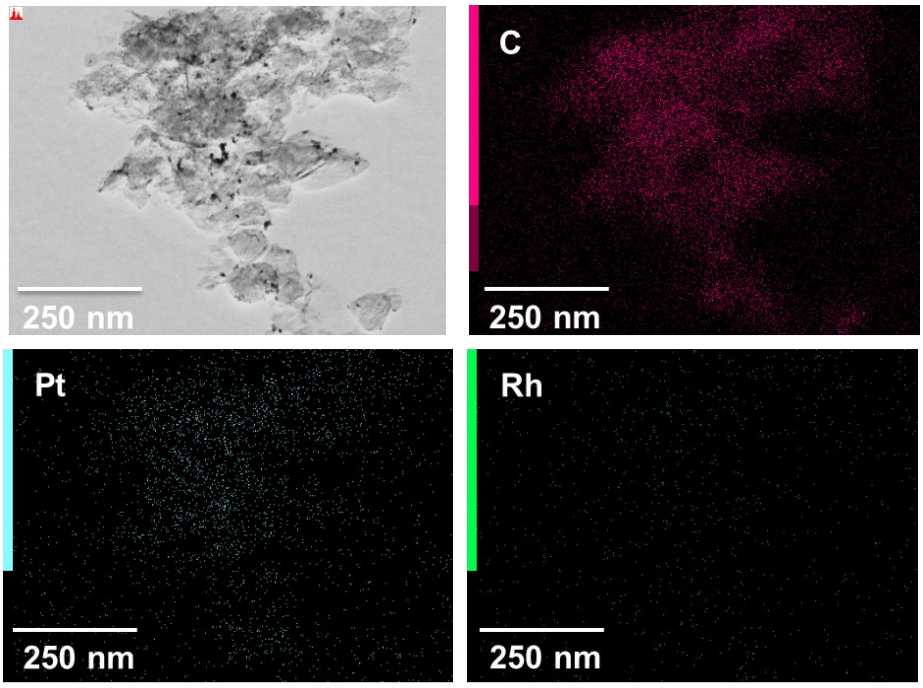

Figure S5 STEM/EDX mapping of the PtRh(nP)/nC composite materials. STEM images in the top left, mapping of the carbon edge in the top right (red) and the respective metal edge Pt (blue, bottom left side) and Rh (green, bottom right side).

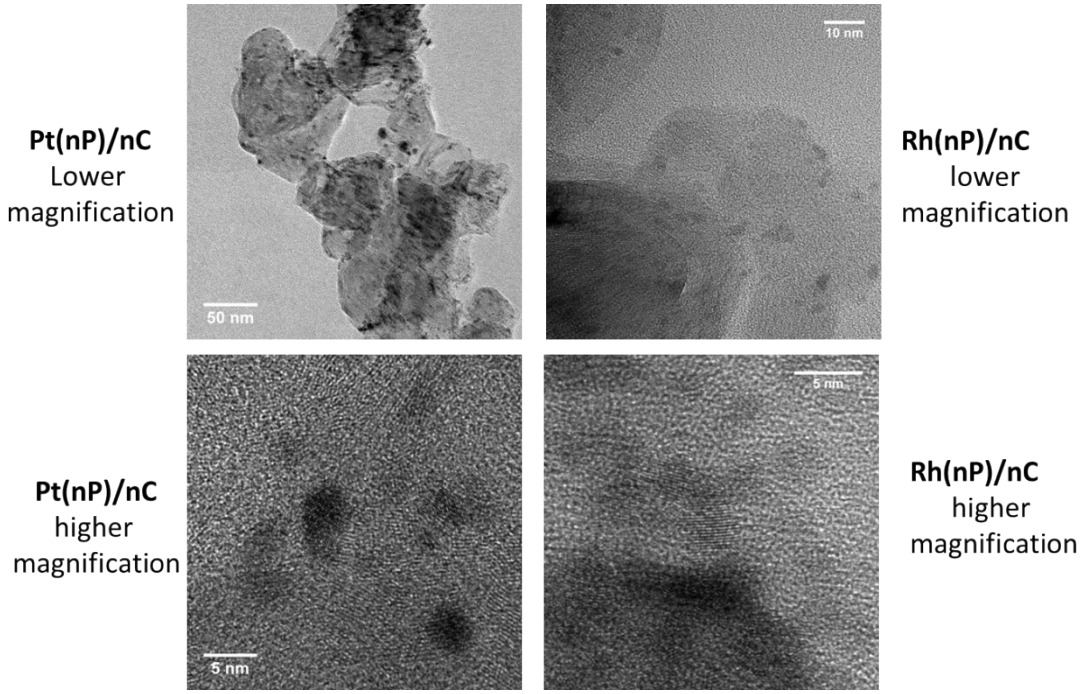

Figure S6 HR-TEM images of the Pt(nP)/nC (left side) and Rh(nP)/nC (right side) composite material. Lower magnification overview images in the top and higher magnification pictures showing the atomic planes of the nanoparticles in the bottom.

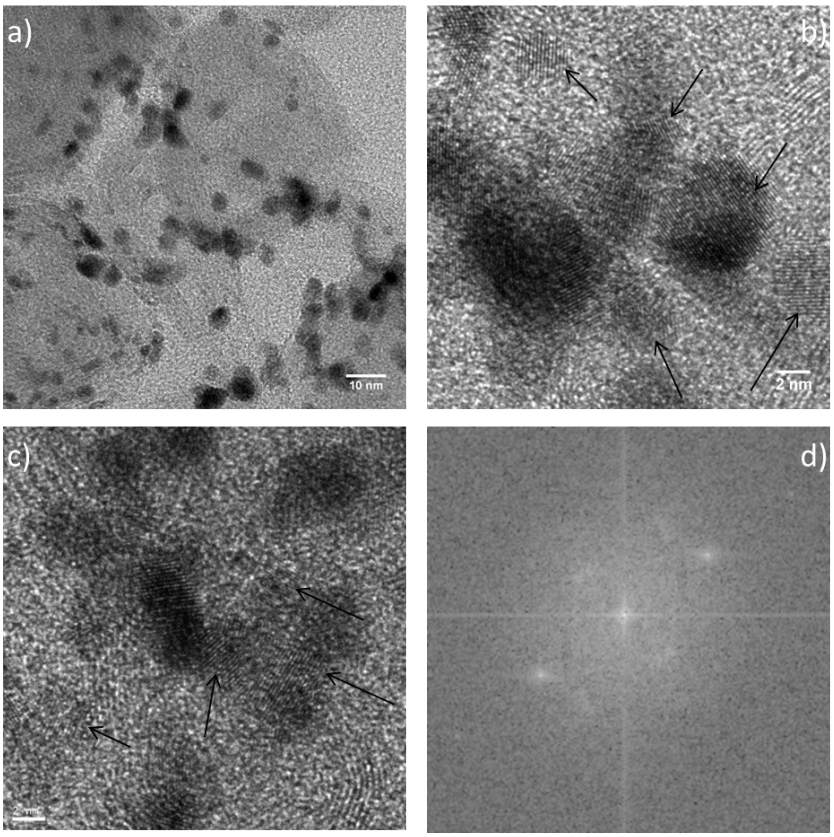

7 HR-TEM images of the Pt(nP)/nC a) lower magnification b), c) higher magnification image and d) corresponding diffraction pattern of the nanoparticles. Some of the nanoparticle in the image have been marked by arrows to guide the viewers eye.

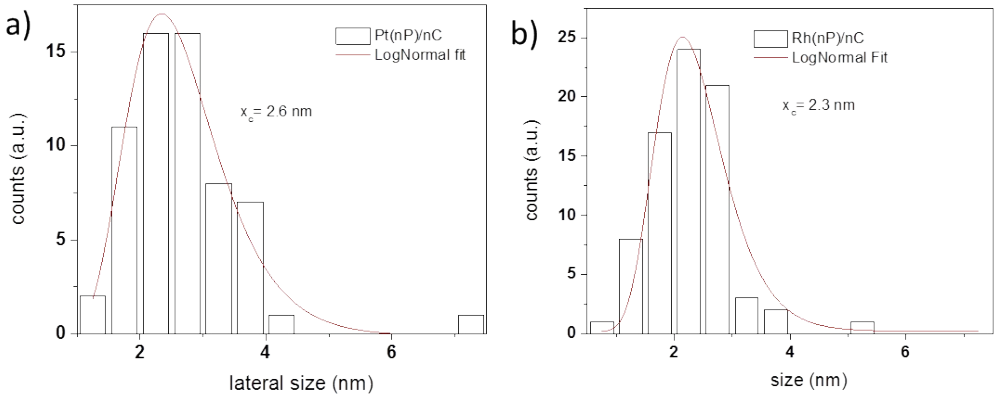

Figure S8 Analysis of the distribution of sizes of the nanoparticles of a) Pt(nP)/nC, b) Rh(nP)/nC composite materials based on the analysis of about 20 HR-TEM images and the size measurements of 62 nanoparticles for the former and 77 nanoparticles for the latter case.

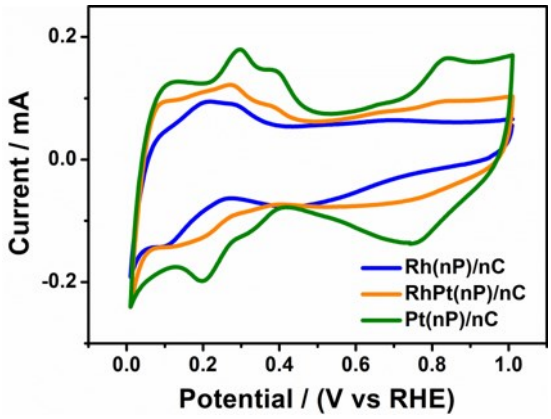

Figure S9 CV polarization curves of Rh(nP)/nC, RhPt(nP)/nC and Pt(nP)/nC at a scan rate 50 mV s^{-1} in 0.1 M KOH solution.

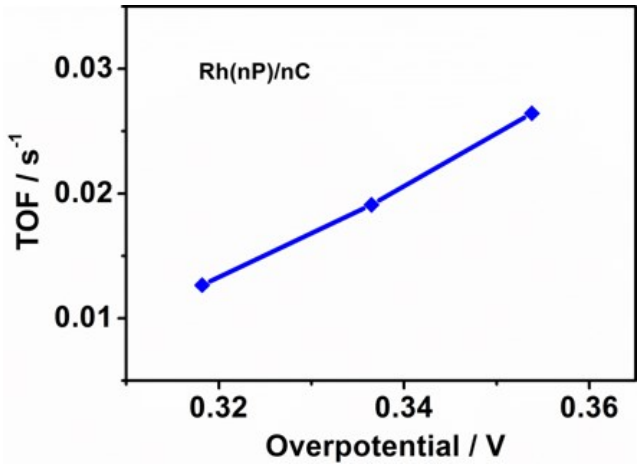

Figure S10 TOF values of Rh(nP)/nC for the OER calculated from 200 seconds potential steps at overpotentials of 318 mV, 336 mV, and 354 mV, respectively.

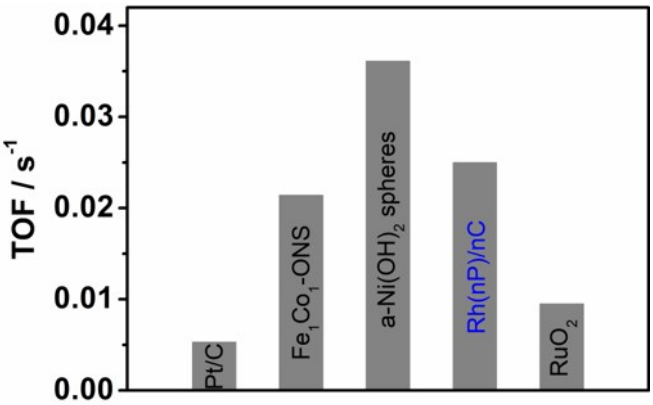

Figure S11 Comparation of TOF values of Rh(nP)/nC with materials reported in recent literatures[4,5] for the OER in 0.1 M KOH solution at overpotential of 350 mV.

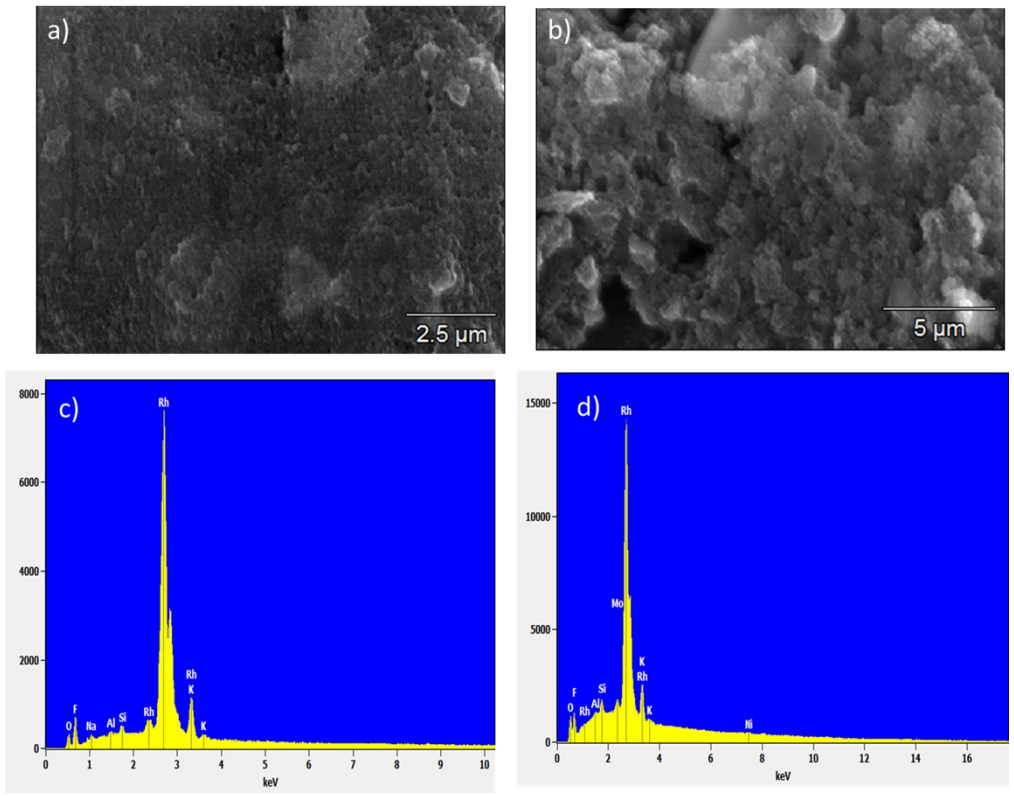

Figure S12 SEM images of the Rh(nP)/nC a) before and after b) electrolysis with respective EDX measurements on c), d).

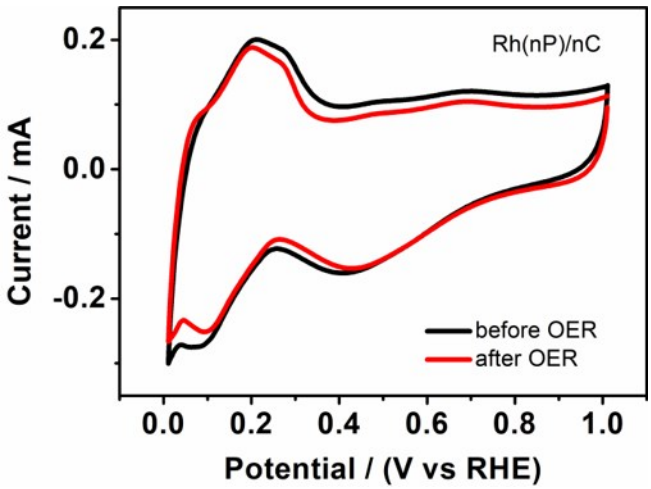

Figure S13 CV polarization curves of Rh(nP)/nC at a scan rate 50 mV s^{-1} in 0.1 M KOH solution.

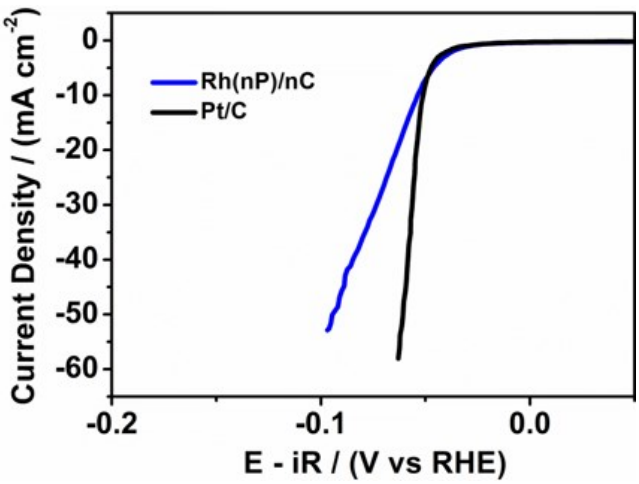

Figure S14 HER performances of Rh(nP)/nC and the commercial Pt/C in 0.5 M H_2SO_4 solution.

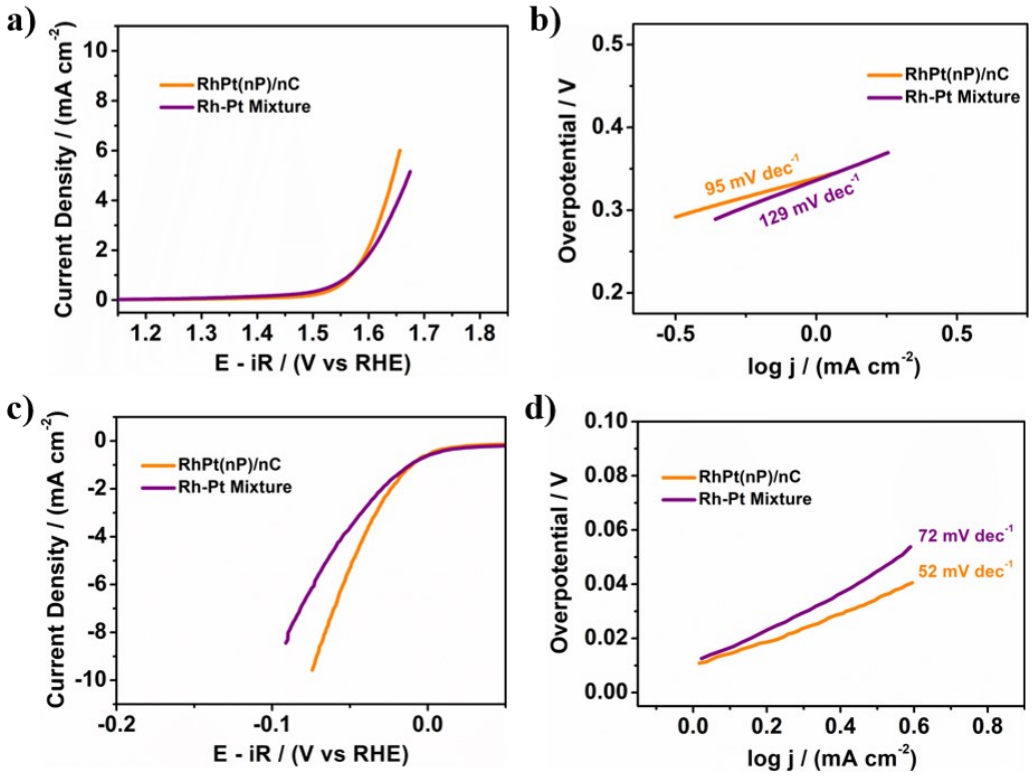

Figure S15 Comparation of a) and b) OER, c) and d) HER performances of Rh-Pt mixture with RhPt(nP)/nC in alkaline solution.

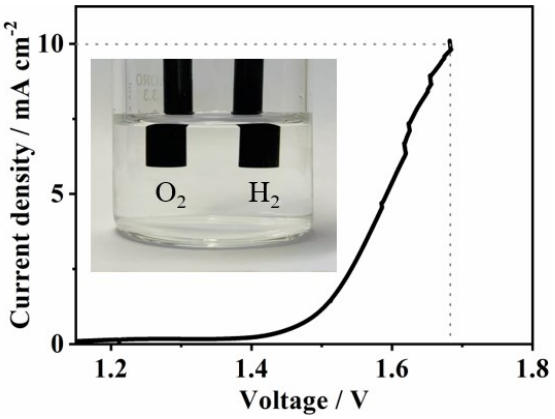

Figure **S16** Overall water splitting curve of Rh(nP)/nC||Rh(nP)/nC couple at a scan rate of 2 mV s^{-1} in 0.1 M KOH. The inset shows an optical photograph of the two-electrode electrolyzer measurement.

Table ST2. Comparison of the OER performance of Rh(nP)/nC in alkaline medium with previous works.

Catalysts	Electrolytes	Overpotential (mV) at 10 mA cm^{-2}	Tafel slope (mV dec^{-1})	Ref.
Rh NSs	0.1 M KOH	380	96.8	[6]
Commercial Rh/C	0.1 M KOH	532	110.8	[6]
Commercial Pt/C	0.1 M KOH	755	245.0	[6]
$Pt/CaMnO_3$	0.1 M KOH	570	-	[7]
$Cu_{0.3}Ir_{0.7}O_{\delta}$	0.1 M KOH	415	-	[8]
$Pt\text{-}LiCoO_2$	0.1 M KOH	440	87	[9]
Cu_3P NB	1.0 M KOH	380	-	[10]
Fe_2O_3 HNR/CNT	1.0 M KOH	383	68	[11]
Co_3O_4-BCN	1.0 M KOH	394	-	[12]
$Ni_xFe_{3-x}O_4$	1.0 M KOH	402	53	[13]
(Fe, V, Co, & Ni)-MnO_2	1.0 M KOH	390	104.4	[14]
Rh(nP)/nC	0.1 M KOH	379	123	This work

NS: nanosheet; NB: nanobush; HNR: hollow nanorods; CNT: carbon nanotube; BCN: boron carbon nitride;

Table ST3. The HER performance of Rh(nP)/nC in alkaline medium compared with other reported catalysts.

Catalysts	Electrolytes	Overpotential (mV) at 10 mA cm^{-2}	Tafel slope (mV dec^{-1})	Ref.
$Rh/C_3N_4/C$	0.1 M KOH	79	-	[15]
$Rh\text{-}Rh_2O_3$-NPs/C	0.5 M KOH	63	70	[16]
Commercial Pt/C	0.5 M KOH	103	113	[16]
Commercial Rh/C	0.5 M KOH	150	116	[16]
$FePSe_3$/NC	1.0 M KOH	118.5	88	[17]
Co-Fe-P	1.0 M KOH	86	66	[18]
CoNiP@NF	1.0 M KOH	155	115	[19]
CoP/Ni_5P_4 /CoP	1.0 M KOH	71	58	[20]
CoP-FeP	1.0 M KOH	163	51.2	[21]
$Rh_{50}Ru_{50}$@UiO-66-NH_2	1.0 M KOH	177	111.8	[22]
Rh(nP)/nC	0.1 M KOH	71	50	This work

NP: nanoparticles; NC: N-doped carbon; NF: nickel foam;

References

1 F. Hof, K. Kampioti, K. Huang, C. Jaillet, A. Derré, P. Poulin, H. Yusof, T. White, K. Koziol, C. Paukner and A. Pénicaud, *Carbon*, 2017, **111**, 142–149.

2 E. Verlato, S. Barison, Y. Einaga, S. Fasolin, M. Musiani, L. Nasi, K. Natsui, F. Paolucci and G. Valenti, *J. Mater. Chem. A*, 2019, **7**, 17896–17905.

3 T. J. P. Hersbach, R. Kortlever, M. Lehtimäki, P. Krtil and M. T. M. Koper, *Phys.Chem.Chem.Phys.*, 2017, **19**, 10301–10308.

4 M. Gao, W. Sheng, Z. Zhuang, Q. Fang, S. Gu, J. Jiang and Y. Yan, *J. Am. Chem. Soc.*, 2014, **136**, 7077−7084.

5 L. Zhuang, L. Ge, Y. Yang, M. Li, Y. Jia, X. Yao and Z. Zhu, *Adv. Mater.*, 2017, **29**, 1606793.

6 N. Zhang, Q. Shao, Y. Pi, J. Guo and X. Huang, *Chem. Mater.*, 2017, **29**, 5009–5015.

7 X. Han, F. Cheng, T. Zhang, J. Yang, Y. Hu and J. Chen, *Adv. Mater.*, 2014, 26, 2047–2051.

8 W. Sun, Y. Song, X. Q. Gong, L. M. Cao and J. Yang, *Chem. Sci.*, 2015, **6**, 4993–4999.

9 C. Su, T. Yang, W. Zhou, W. Wang, X. Xu and Z. Shao, *J. Mater. Chem. A*, 2016, **4**, 4516–4524.
10 S. Wei, K. Qi, Z. Jin, J. Cao, W. Zheng, H. Chen and X. Cui, *ACS Omega*, 2016, **1**, 1367–1373.
11 H. A. Bandal, A. R. Jadhav, A. A. Chaugule, W. J. Chung and H. Kim, *Electrochim. Acta*, 2016, **222**, 1316–1325.
12 T. Balakrishnan, M. Anis, S. Arun, M. Kumar, S. Arun Kumar and S. Mayavan, *RSC Adv.*, 2016, **6**, 79448–79451.
13 Y. Feng, J. Wei and Y. Ding, *J. Phys. Chem. C*, 2016, **120**, 517–526.
14 Z. Ye, T. Li, G. Ma, Y. Dong and X. Zhou, *Adv. Funct. Mater.*, 2017, **27**, 1704083.
15 Y. Zheng, Y. Jiao, Y. Zhu, L. H. Li, Y. Han, Y. Chen, M. Jaroniec and S. Z. Qiao, *J. Am. Chem. Soc.*, 2016, **138**, 16174–16181.
16 M. K. Kundu, R. Mishra, T. Bhowmik and S. Barman, *J. Mater. Chem. A*, 2018, **6**, 23531–23541.
17 J. Yu, W. J. Li, H. Zhang, F. Zhou, R. Li, C. Y. Xu, L. Zhou, H. Zhong and J. Wang, *Nano Energy*, 2019, **57**, 222–229.
18 J. Chen, J. Liu, J. Q. Xie, H. Ye, X. Z. Fu, R. Sun and C. P. Wong, *Nano Energy*, 2019, **56**, 225–233.
19 A. Han, H. Chen, H. Zhang, Z. Sun and P. Du, *J. Mater. Chem. A*, 2016, **4**, 10195–10202.
20 I. K. Mishra, H. Zhou, J. Sun, F. Qin, K. Dahal, J. Bao, S. Chen and Z. Ren, *Energy Environ. Sci.*, 2018, **11**, 2246–2252.
21 Y. Du, Z. Wang, H. Li, Y. Han, Y. Liu, Y. Yang, Y. Liu and L. Wang, *Int. J. Hydrogen Energy*, 2019, **44**, 19978–19985.
22 Z. Ding, K. Wang, Z. Mai, G. He, Z. Liu and Z. Tang, *Int. J. Hydrogen Energy*, 2019, **44**, 24680–24689.